Full length article

Atom probe tomography study of Fe-Ni-Al-Cr-Ti ferritic steels with hierarchically-structured precipitates

Sung-Il Baik [a, b, *], Michael J.S. Rawlings [a], David C. Dunand [a]

[a] Department of Materials Science & Engineering, Northwestern University, Evanston, IL 60208, USA
[b] Northwestern University Center for Atom-Probe Tomography, Evanston, IL 60028, USA

ABSTRACT

The ferritic Fe-Ni-Al-Cr-Mo steel (FBB8) has good creep properties up to 700 °C due to B2-NiAl nanoscale precipitates and its creep resistance can be further improved by additions of 2 or 4 wt.% Ti, as a result of sub-precipitates within the main precipitates. Here, the hierarchical structure of the precipitates is studied in the light of phase separation via transmission electron microscopy (TEM) and atom probe tomography (APT). For FBB8-2Ti (with 2% Ti added) exhibiting B2-NiAl precipitates with L2$_1$-Ni$_2$AlTi sub-precipitates, APT analysis shows strong partitioning of Ni, Al and Ti from the ferritic matrix into the B2/L2$_1$ precipitates and, within the precipitates, partitioning of Ti and Fe within the L2$_1$ sub-precipitates. Based on the published pseudo-binary phase-diagram between (Ni,Fe)Al and (Ni,Fe)Ti, this hierarchical precipitate microstructure is discussed based on the known miscibility gap between the B2 and L2$_1$ phases, due to partitioning of Ti into the L2$_1$ phase and ordering of Al and Ti on the Al sub-lattice of the B2 structure. For FBB8-4Ti (with 4% Ti added), by contrast, the L2$_1$ precipitates exhibit bcc sub-precipitates rich in Fe and Cr, with a composition close to that of the matrix; the absence of the B2 structure is consistent with an increase of Ti and Fe concentrations, to 18.2 and 19.3 at.% respectively, as measured via APT, in the L2$_1$ precipitates.

© 2017 Acta Materialia Inc. Published by Elsevier Ltd. All rights reserved.

1. Introduction

Precipitate-strengthened ferritic steels are an attractive alternative to austenitic steels and Ni-based superalloys for high-temperature and -stress applications due to their lower cost, lower thermal expansion, and higher thermal conductivity [1–3]. The precipitates generally consist of carbides, nitrides, and/or intermetallic compounds such as Laves, μ, η, σ phases [4–7]. However, theses precipitation strengthened ferritic steels have a use temperatures limited to 600 °C, because of their weak oxidation resistance and creep strength deterioration during long-term operation [8–11]. Unlike carbide and Laves precipitates-strengthened ferritic alloys for steam-turbine applications, the present ferritic alloys are strengthened by hierarchical structured precipitates consisting of L2$_1$-Ni$_2$AlTi sub-precipitate within B2-NiAl precipitates or bcc sub-precipitate within L2$_1$-Ni$_2$AlTi precipitates, which are oxidation- and coarsening resistant [12,13]. The

hierarchical nature of the B2/L2$_1$ precipitate increases the creep resistance by making dislocation shear of the two-phase precipitates more difficult, and by increasing the lattice misfit with the matrix, resulting in a strain field that more effectively traps dislocations on the arrival or departure sides of the precipitates [14,15].

The presence of a miscibility gap between bcc-Fe and B2-NiAl in the Fe−Ni−Al system enables precipitation hardening in the bcc-Fe matrix phase by coherent B2-ordered NiAl precipitates [16–18]. Jiang et al. [19] proposed a strategy for the design of ultra-high strength alloy via high-density B2-phase nano-precipitation with minimal lattice misfit in the coherent interface with the bcc matrix. Low lattice misfit (0.03 ± 0.04%) decreases the nucleation barrier for precipitation, which can stabilize nano-precipitates (~2.7 ± 0.2 nm) with a high number density (>10^{24} m^{-3}). A high anti-phase boundary (APB) energy increases the ordering hardening of alloy by increasing dislocation shear resistance in the precipitate. However, the low misfit between precipitate and matrix is not effective in high temperature applications because the creep mechanisms in these ferritic steels strengthened by B2-ordered NiAl precipitate are not shear, but rather dislocation climb and repulsive elastic interaction between precipitates and

matrix dislocations [20,21]. The addition of titanium to these steels significantly improves their creep resistance up to ~179 MPa from ~69 MPa at 700 °C through the creation of the L2$_1$-Ni$_2$AlTi phase [15,20,22]. Replacing half of the Al atoms with Ti in the B2-NiAl phase results in the Heusler-phase, L2$_1$-Ni$_2$TiAl, which provides greater creep resistance than B2-NiAl by increasing the lattice parameter mismatches between the ferritic matrix and the ordered precipitates [23,24]. The lattice parameter of ternary, stoichiometric L2$_1$-Ni$_2$TiAl, 0.5895 nm [25] is 2% larger than twice the lattice parameter of B2-NiAl, 0.2887 nm [26]. This lattice misfit is sufficiently low to allow for a semi-coherent or coherent Heusler-phase precipitate structure within the bcc-ferritic matrix. Due to their high thermodynamic stability at temperatures [18,27] and low coarsening rate above 700 °C [28], these B2 and L2$_1$ precipitates are good substitutes for typical carbides and Laves precipitates. Furthermore, they maintain their strengthening even for long aging time, e.g., up to ~30 days at 700 °C [15]. The addition of Al (over ~2.5 at.%) in the alloy suppresses the ferrite (bcc) to austenite (fcc) phase transformation that can limit their use at an elevated temperature [29,30]. Then, coherent B2 phase and L2$_1$ sub-phase are nucleated from the stable bcc structure at elevated temperature.

For the fcc structured Ni-based alloy, L1$_2$ ordered-γ′ precipitates are coherent with the fcc - γ matrix, and Ti addition delays their coarsening by inducing splitting of the precipitates during aging [31–33]. In this phenomenon of inverse coarsening, the γ′ precipitates serve as a matrix for γ sub-precipitates, resulting in a hierarchical microstructure consisting of γ matrix containing γ′ precipitates which themselves contain γ sub-precipitates [34]. In Ni-Al-Ti-based ferritic steels, the precipitation behavior is complicated by the presence of three phases: B2, L2$_1$ and α-bcc. The morphology and kinetic evolution of hierarchical microstructures within the precipitate of a Ni-Al-Ti ferric alloy were mainly studied by transmission electron microscopy (TEM) [13,35]. The hierarchical microstructure is, however, sensitive to the alloy Ti concentration by ordering process in B2-NiAl phase [18,31]. Three-dimensional (3D) atom probe tomography (APT) is a unique analytical instrument suited for the study at such complex nano-precipitates, as it allows for site-specific analysis of chemical heterogeneities of matrix and precipitates with atomic scale spatial resolution [36–39].

Here, we present a study of microstructural and chemical evolution for two types of hierarchical microstructures in ferritic Fe-Ni-Al-Cr-Mo steels modified with 2 and 4% Ti, utilizing transmission electron microscopy (TEM) and atom probe tomography (APT). Understanding the sub-precipitate formation within the main precipitates will help with a further rational alloying design of these steels to achieve higher strength and creep resistance, by tailoring the lattice parameter mismatches between matrix, precipitates and sub-precipitates, as well as the volume fraction, shape, anti-phase boundary energy and hierarchy of the precipitated phases.

2. Experimental procedures

Two ferritic steels were prepared by arc-melting, with compositions measured by direct-current plasma mass spectroscopy at ATI Wah Chang (Albany, OR): Fe-10.2Ni-5.8Al-10.4Cr-3.1Mo-0.26Zr-0.001B-2.0Ti (wt.%) labeled FBB8+2Ti and Fe-10.4Ni-5.4Al-10.0Cr-3.5Mo-0.18Zr-0.005B-4.0Ti (wt.%) labeled FBB8-4Ti; the composition in at.% are, Fe-8.94Ni-11.39Al-10.49Cr-1.82Mo-0.25Zr-0.005B-2.21Ti and Fe-9.41Ni-10.93Al-10.31Cr-1.86Mo-0.25Zr-0.005B-4.22Ti, respectively. The cast ingots were homogenized at 1200 °C for 0.5 h in evacuated quartz tubes, air-cooled, aged at 700 °C for 100 h in air and air-cooled on a ceramic block.

TEM samples were cut using a rotary disc cutter in the polished surface. The 3 mm diameter discs were ground to ~100 μm in thickness and further thinned to electron transparency using an electrolyte of 10% perchloric acid in ethanol bath at a temperature of −30 °C. Bright field (BF) and super-lattice dark-field (DF) TEM imaging was performed in a H8100 (Hitachi) microscopes operated at 200 kV.

Atom probe nanotips were prepared by electropolishing using 10% perchloric acid and ethanol electrolyte. Using a local electrode atom probe (LEAP) tomograph (4000X-Si), pulses of ultraviolet laser light (355 nm wavelength) were applied to the nanotips at a pulse repetition rate of 500 kHz, with 20–30 pJ per pulse, under ultrahigh vacuum ($<2 \times 10^{-11}$ Torr), at a temperature at 50.0 ± 0.3 K. The times of flight of the detected ions (average detection rate of 0.01 ions per pulse) were used to produce three-dimensional (3-D) reconstructions using the program IVAS (version 3.6.8). The concentration of Al$^+$ is overlapped with Fe^{2+} at 27 Da in the APT mass spectrum, and it is corrected by extraction of isotopic ratio of Fe at 27 Da. Compositional information was obtained employing the proximity histogram methodology for APT [40].

3. Results

3.1. TEM results of hierarchical microstructure in precipitate

The precipitate structure after aging at 700 °C for 100 h was investigated utilizing bright field (BF) and dark-field (DF) transmission electron microscopy (TEM) images with selected area diffraction pattern (SADP), Fig. 1. BF and DF images are taken in the near [10$\bar{1}$] zone axis orientation with transmitted beam, (000), for BF and (111) for DFs in the B2-ordered NiAl and L2$_1$-ordered Ni$_2$TiAl precipitates in the FBB8-2Ti and -4Ti alloys. The SADP in Fig. 1a
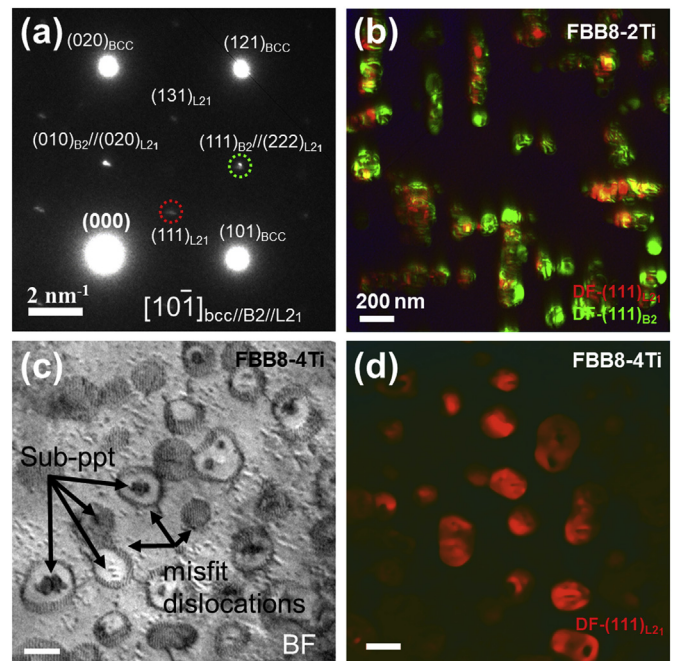
Fig. 1. Transmission electron microscopy (TEM) analyses of FBB8-2Ti (a–b) and FBB8-4Ti (c–d) aged at 700 °C for 100 h. (a) Selected area diffraction pattern (SADP) with the [10$\bar{1}$] zone axis for FBB8-2Ti and - 4Ti alloys, (b) mixed dark field (DF) image of (111) reflection of B2 precipitates (green color) and (111) reflection of L2$_1$ sub-precipitate (red color) in FBB8-2Ti alloy, (c) bright field (BF) image and (d) dark field (DF) image of (111) reflection of L2$_1$ precipitates in FBB8-4Ti alloy. (For interpretation of the references to colour in this figure legend, the reader is referred to the web version of this article.)
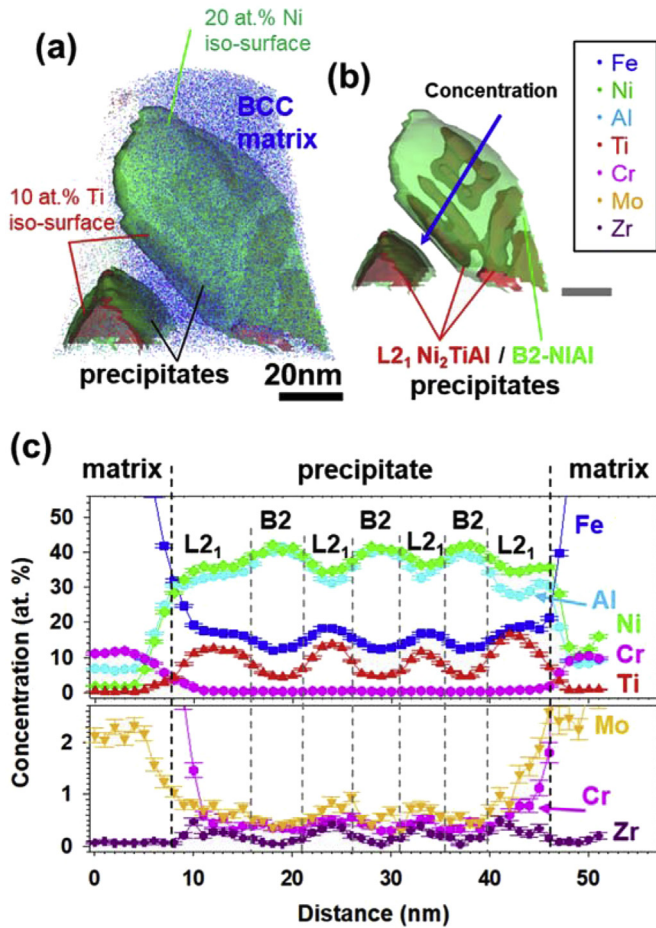
Fig. 2. Atom probe tomography (APT) analysis of hierarchical B2/L2$_1$ precipitates in FBB8-2Ti. (a) 3D reconstruction of volume showing Al, Ni, Fe, Cr, Mo, Zr, and Ti and two iso-(concentration) surfaces of 20 at.% Ni (green color) and 10 at.% Ti (red color), (b) 3D reconstruction of hierarchical precipitates with transparent Ni and Ti iso-surfaces. (c) Concentration profiles of Al, Ni, Fe, Cr, Mo, Zr, and Ti created using a 0.5 nm bin size along the blue arrow across the B2 precipitate containing L2$_1$ sub-precipitates in (b). The vertical dotted lines are placed to indicate the location of the (bcc)/L2$_1$ and B2/L2$_1$ interfaces. (For interpretation of the references to colour in this figure legend, the reader is referred to the web version of this article.)

clearly reveals the presence of super-lattice reflections corresponding to both B2- and L2$_1$-ordered phases (010 and 111) and unique L2$_1$-ordered Ni$_2$TiAl (111 and 131). The three structures, bcc, B2 and L2$_1$, have cube-on-cube crystallographic orientation relationships, maintaining coherent or semi-coherent interfaces. Replacing half of the Al atoms with Ti in the B2 ordered NiAl phase results in the L2$_1$ ordered Ni$_2$TiAl, hence the unit-cell of L2$_1$-phase is double the unit-cell of B2-NiAl with slight volume changes. As a

results, the (020) and (222) planes of the L2$_1$ phase overlap with the (010) and (111) planes of the B2 phase in the SADP.

The precipitates in Fig. 1b, displayed in the DF image of (111)$_{B2}$ and (111)$_{L21}$ super-lattice of the FBB8-2Ti alloy, show a cuboidal shape with width ranging from 50 to 100 nm. The regions of red color in the DF image, Fig. 1b, represent L2$_1$ sub-precipitates embedded within B2 precipitates with green color. The matrix-precipitate and the B2-L2$_1$ interfaces are observed to be coherent with an interfacial alignment towards a cube-on-cube orientation. The bright-field (BF) and DF images of the FBB8-4Ti alloy, Fig. 1c and d, shows L2$_1$-ordered precipitates with a spherical and/or ellipsoidal shape with diameters between 200 and 500 nm. The dark regions in the L2$_1$ precipitate were identified as Fe-rich bcc plates [24]. The averaged lattice misfits between bcc-Fe and L2$_1$ phases in FBB8-4Ti, determined by neutron diffraction (ND), is 1.32% at 973 K, which is larger than that of precipitate in FBB8-2Ti (0.77%) [41]. The larger lattice misfit causes the formation of misfit dislocations at the interface between the Fe matrix and L2$_1$ precipitate in the FBB8-4Ti alloy, Fig. 1c. The shape change from cuboidal in FBB8-2Ti to spheroidal in FBB8-4Ti is also expected to be due to loss of coherency, confirmed by the presence of a misfit dislocation network at the matrix-precipitate interface in BF image [15,27]. Precipitate alignment with the matrix along <100> occurs in FBB8-2Ti but precipitate alignment is not present in FBB8-4Ti, with its incoherent interface; this is consistent with lattice misfit driving precipitate alignment, rather than interfacial energy effects. In summary, the TEM microstructural observation confirms the prior results [15,35] that the single-phase B2 precipitates present in FBB8 [20] are changed, upon Ti addition, to hierarchical B2/L2$_1$ for FBB8-2Ti and L2$_1$/bcc for FBB8-4Ti.

3.2. Hierarchical L2$_1$/B2 precipitates

Fig. 2a displays a 3D APT reconstruction of FBB8-2Ti with 20.5 million ions showing B2 and L2$_1$ precipitates given by green Ni and red Ti iso-(concentration) surface envelopes, respectively. Iso-surface represents the average of the far-field plateau concentrations of the two phases, by employing the inflection-point methodology [42]. With iron atoms displayed as blue dots, the Fe-rich bcc matrix appears blueish despite the presence of other elements. Fig. 2b shows an extracted iso-surface image of the hierarchical precipitates with transparent green Ni and red Ti iso-surfaces. The larger B2 (green iso-surface) precipitate in the upper right side of the reconstruction shows a complex hierarchical microstructure with plate-shaped L2$_1$ sub-precipitates (red iso-surface). These L2$_1$ sub-precipitates are crystallographically aligned (along the <001> direction, as identified in TEM experiments), which suggests a strong effect of coherency stresses on the interface [43]. It is known that the precipitate structures can be tailored via heat treatment in FBB8-2Ti. In a fast cooling process with melt-spinning technique, single-phase B2 precipitates are obtained, with the hierarchical L2$_1$

Table 1
Composition (at. %) of FBB8-2Ti alloy (measured by direct-current plasma mass spectroscopy after casting) and of constitutive phases, matrix, B2 and L2$_1$ (after aging treatment at 700 °C for 100 h, as determined by atom probe tomography). Uncertainties are represented by the standard deviation (σ) from the counting statistics measurement series (at.%). Partitioning ratios and their errors (sum of relative errors of concentration) are also given.

Phase	Fe	Ni	Al	Ti	Mo	Cr	Zr
Nominal composition	64.96	8.94	11.39	2.21	1.82	10.49	0.15
Matrix (bcc)	76.16 ± 0.43	1.77 ± 0.13	6.56 ± 0.25	0.35 ± 0.06	2.15 ± 0.13	12.52 ± 0.02	0.07 ± 0.02
Precipitate (B2)	14.26 ± 0.37	40.02 ± 0.49	37.53 ± 0.46	6.76 ± 0.06	0.55 ± 0.07	0.37 ± 0.06	0.10 ± 0.03
Partitioning ratio (B2/bcc)	0.2 ± 0.01	23.2 ± 1.7	6.0 ± 0.3	13.1 ± 2.5	0.2 ± 0.03	0.03 ± 0.01	1.4 ± 0.3
Sub-precipitate (L2$_1$)	17.42 ± 0.46	35.71 ± 0.54	32.22 ± 0.51	13.13 ± 0.38	0.91 ± 0.11	0.63 ± 0.09	0.34 ± 0.07
Partitioning ratio (L2$_1$/bcc)	0.2 ± 0.01	20.2 ± 1.5	4.9 ± 0.2	37.0 ± 2.5	0.4 ± 0.06	0.06 ± 0.01	4.9 ± 0.5
Partitioning ratio (L2$_1$/B2)	1.4 ± 0.1	0.9 ± 02	0.8 ± 0.02	2.8 ± 0.2	2.0 ± 0.4	1.9 ± 0.4	3.4 ± 1.2

sub-precipitates being formed within the B2 precipitates only during a subsequent aging treatment [13]. On the other hand, the L2$_1$ phase is reported as a major phase in the hierarchically-structured precipitates following homogenization at 1200 °C and air cooling [14]. The initial phase and the subsequent evolution of the precipitate substructure, which underlies the hierarchical microstructures, are strongly influenced by the B2/L2$_1$ phase equilibria in the pseudo-binary Ni(Al$_{1-x}$Ti$_x$) system [13,18]. In the pseudo-binary NiAl-NiTi phase diagram, the majority phase is given by the Ti concentration and its ordering state [18]. L2$_1$-Ni$_2$TiAl is formed by ordering of Ti, replacing half the Al atoms in the B2-NiAl phase; however, incomplete ordering with a low amount of Ti results in the two-phase decomposition (B2 and L2$_1$). This point is discussed in a later section.

A one-dimensional (1-D) concentration profile across the precipitate of FBB8-2Ti is shown in Fig. 2c, using a 0.5 nm bin size along the blue arrow across the hierarchical B2/L2$_1$ precipitate shown in the 3D reconstruction image of Fig. 2b; the 2σ error is equal to the statistical variance of values from different 3-D volumes [44]. The compositions, as determined by APT time-of-flight (TOF) analysis, of the Fe-rich bcc matrix and of the B2, and L2$_1$ precipitate are summarized in Table 1. It is apparent that Fe, Cr and Mo are strongly partitioned in the matrix, whereas Ni, Al, Ti and Zr are mainly concentrated in the B2 and L2$_1$ sub-precipitates. The ratios of concentrations of a solute element between two immiscible phases at equilibrium is represented as a partitioning coefficient (P) [45], also included in Table 1. The partitioning ratios of Ni ($C_{Ni}^{ppt}/C_{Ni}^{matrix}$) are 23.2 ± 1.7 for the B2 phase and 20.2 ± 1.5 for the L2$_1$ phases. Ti partitioning ratios are also high, with values of 13.1 ± 2.5 and 37.0 ± 2.5 in the B2 and L2$_1$ phases, respectively. The partitioning of Al is much less than Ni and Ti: 6.0 ± 0.3 and 4.9 ± 0.2 in the B2 and L2$_1$ phases, respectively. Finally, the partitioning ratio of Zr between the L2$_1$ precipitates and the bcc matrix, 4.9 ± 0.2, is larger than that between the B2 precipitates and the bcc matrix. 1.4 ± 0.3. Zirconium is, however, detected at concentration lower (by a factor 0.3) than the nominal composition value, as expected from the formation of a secondary phase (identified as Fe$_{23}$Zr$_6$ with space group Fm-3m) at the grain boundary region [20]. By contrast, Cr and Mo are depleted in the precipitates, with partitioning ratios below unity. From these partitioning ratios, it can be concluded that the precipitate volume fraction is controlled mainly by Ni and Ti and, to a less extent, by Al, for this concentration range of ferritic steel. On the other hand, Cr and Mo can be expected to reduce the volume fraction of precipitates.

The 1-D concentration profile in Fig. 2c shows a concentration fluctuation for the five major elements (Fe, Ni, Al, Ti, and Cr) and the two minor elements (Mo and Zr) across hierarchical B2/L2$_1$ phases in precipitate. Because the L2$_1$-Ni$_2$TiAl phase is formed by replacing half of the Al atoms with Ti in the B2-NiAl phase, these concentration fluctuations can be matched to B2 and L2$_1$ phase separation in DF- TEM analysis, Fig. 1b, of the FBB8-2Ti alloy. Four peaks for Ti and Fe are visible, consistent with L2$_1$ - Ni$_2$TiAl sub-precipitates enriched in these elements, as compared to the B2 precipitate surrounding the sub-precipitate. By contrast, the B2 precipitate is enriched in Ni and Al as compared to the L2$_1$ sub-precipitates: Ni and Al concentrations increases to 42 and 41 at.% in the B2 phase, from 33 to 30 at% in the L2$_1$ phase, respectively. The highest partitioning ratio between the B2 and L2$_1$ phases, among the majority elements (Fe, Ni, Al, Ti and Cr) in the precipitate, is for Ti (2.8 ± 0.2), which favors strongly the L2$_1$ phase as the transition between B2-NiAl and L2$_1$-Ni$_2$TiAl is driven by a replacement of Al with Ti in their sub-lattice sites. Mo, Cr and Zr also partition into the L2$_1$ phase with a value of 2.0 ± 0.4, 1.9 ± 0.4 and 3.4 ± 1.2. However, Al concentration does not drop sufficiently to compensate the increase in Ti concentration and achieve the stoichiometric equilibrium

Ni$_2$TiAl composition. The range of Al and Ti concentration variations will be discussed in the light of the (Ni,Fe)Al - (Ni,Fe)Ti pseudo-binary phase diagram later. Finally, Fe is also preferentially partitioned into the L2$_1$ phase rather than the B2 phase and the sum of Ni and Fe concentrations is nearly 50 at.% in both B2 and L2$_1$ structure which may indicate that the Fe atoms preferentially occupy the Ni sub-lattice in the L2$_1$-Ni$_2$TiAl structure.
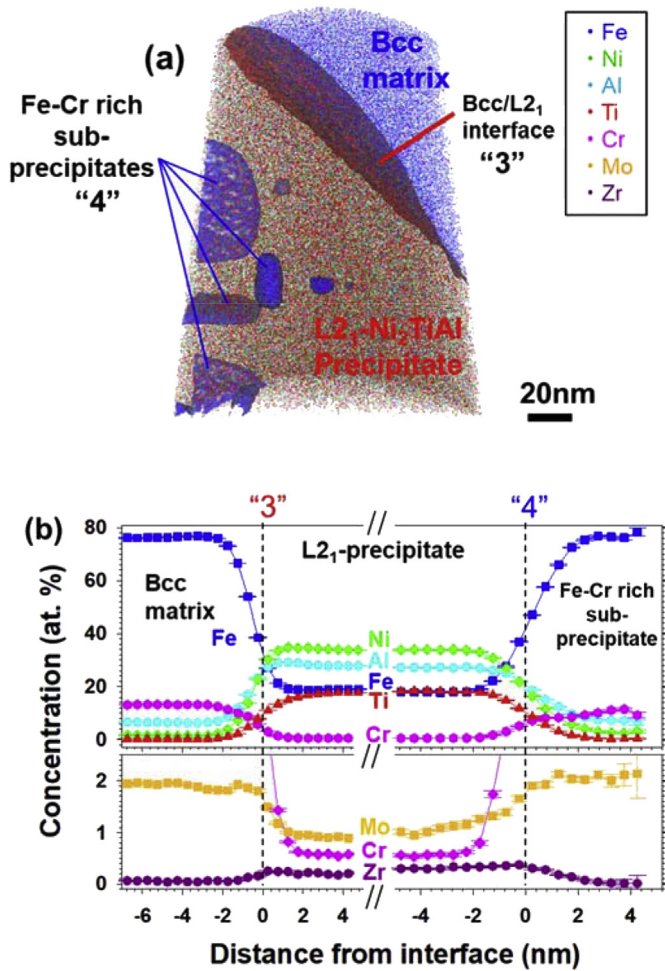
3.3. Hierarchical bcc/L2$_1$ precipitates

Fig. 3 displays a 3D APT reconstruction of the FBB8-4Ti steel with 72 million ions. The reconstructed volume shows bcc matrix, L2$_1$ precipitate and Fe-Cr-rich sub-precipitates within the L2$_1$ precipitate, assumed to have bcc crystal structure, given their composition and TEM analysis. The bcc-matrix is characterized by Fe atoms (blue dots) and is visible in the right-upper corner of the 3D reconstruction. The L2$_1$ precipitate is represented by red-colored iso-surface. The size of the L2$_1$ precipitate is ~200 nm and only part of a precipitate is represented in the lower left part of the 3D APT reconstruction. The Fe-Cr-rich sub-precipitates are represented by blue colored iso-surface within the L2$_1$ precipitate. The Fe-Cr rich precipitates appear to be aligned along specific orientation within the L2$_1$ structure, specifically <001> directions as shown in the TEM results, Fig. 1d.

Concentration profiles straddling the bcc-matrix/L2$_1$-precipitate interfaces and the L2$_1$-precipitate/FeCr-rich sub-precipitate interfaces are presented in Fig. 3b. These concentration profiles were created utilizing the proximity histogram (proxigram) method [40,46] from the bcc-matrix to the L2$_1$ precipitate at the 10 at% Ti iso-surface, marked "3", and from the L2$_1$ precipitate to the FeCr-rich sub-precipitate at the 20 at% Fe iso-surface, marked "4" in Fig. 3a. It is emphasized that these concentration plots contain three-dimensional (3D) information even though this is a two-dimensional (2D) plot. The vertical dotted lines are placed at the inflection points of the measured iso-concentration (10 at.% Ti and 40 at.% Fe) profiles, and indicate the location of the matrix (bcc)/L2$_1$ and L2$_1$/sub-ppts interfaces (marked zero on the abscissa axis). The concentration profile does not show segregation behavior at the interface.

Similar partitioning trends as those reported above for FBB8-2Ti sample are found in these concentration profiles across the bcc-matrix/L2$_1$-precipitate interface. Fe, Cr and Mo are strongly partitioned to the matrix, whereas Ni, Al, Ti and Zr are partitioned to the L2$_1$ precipitate. The elemental concentrations and partitioning ratios are summarized in Table 2. The partitioning ratio of Ti, 50.2 ± 5.3 is much higher than for the matrix/L2$_1$ precipitate in the FBB8-2Ti, 37.0 ± 2.5. The Al concentration also does not reach the stoichiometric concentration of Ni$_2$TiAl-L2$_1$ structure. Both Ti and Fe concentrations, 18.2 ± 0.26 and 19.25 ± 0.27 at.%, in the L2$_1$ precipitates of FBB8-4Ti are somewhat higher than those found in the L2$_1$ phase of FBB8-2Ti, 13.13 ± 0.38 and 17.42 ± 0.46 at.% respectively. As also seen in the FBB8-2Ti sample, the Fe and Ti concentrations are nearly identical in the L2$_1$ phase. Also, the sum of Ni and Fe concentrations is nearly 50 at.%, which is consistent with the preferential occupation of Fe atoms in the Ni sub-lattice of the L2$_1$ structure.

The concentration profile straddling the interface between the L2$_1$ precipitates and the Fe-Cr rich sub-precipitate along the arrow "4" show that, even though the Cr concentration does not quite reach the value found in the matrix (11.55 ± 0.49 vs. 13.08 ± 0.21 at.%), all other elements show nearly the same values of concentration as those of the bcc matrix. This means the hierarchical Fe-Cr rich sub-precipitate within the L2$_1$ precipitate are matrix-like in terms of concentration and thus crystal structure. The intermediate B2 structure with high Ni and Al and

Fig. 3. APT analysis of hierarchical precipitates in FBB8-4Ti. (a) 3D reconstruction of an APT volume showing the bcc matrix, part of a L2$_1$ precipitate and several Fe-Cr rich sub-precipitates within the L2$_1$ precipitate. The L2$_1$ phase is defined by 10 at.% Ti (red color) iso-surfaces and the Fe-Cr rich phase is defined by 20 at.% Fe (blue color) iso-surfaces. (b) Concentration profiles from matrix to L2$_1$ precipitate and from L2$_1$ precipitate to its imbedded sub-precipitates. The concentration profiles were created utilizing a proximity histogram (proxigram) method [40] from the bcc-matrix to L2$_1$ precipitate at the 10 at% Ti iso-surface, marked "3", and from the L2$_1$ precipitate to FeCr-rich sub-precipitate at the 20 at% Fe iso-surface, marked "4" in figure a. (For interpretation of the references to colour in this figure legend, the reader is referred to the web version of this article.)

concentrations is absent, unlike in the FBB8-2Ti sample. As the size of the Fe-Cr rich sub-precipitate increases inside the L2$_1$ precipitate during aging, they may eventually split the L2$_1$ precipitate in a process known as "inverse coarsening" observed in a Ni-based superalloy [34]. For the present again condition, the full separation of L2$_1$ precipitate has not occurred yet; however the growth of sub-precipitate with the same composition as the matrix within

primary precipitates can counter the coarsening of these primary precipitates by splitting, thus preventing the degradation of mechanical properties at high temperature at long aging times.

4. Discussion

4.1. Volume fraction measurement in lever-rule diagram

The APT concentration measurements of precipitates and matrix enable a determination of precipitate volume fraction. When ignoring the sub-precipitates and assuming the alloying elements are evenly partitioned to every precipitate, the volume fraction of precipitates ($V_{f,\beta}$) can be found by the lever rule from the measured concentrations;

$$V_{f,\,\beta} = \frac{C_o - C_\alpha}{C_\beta - C_\alpha} \tag{1}$$

where C_o, C_α and C_β are the compositions of the overall alloy, the matrix and the precipitates, respectively. For each element, the difference between the overall alloy concentration and the matrix concentration (C_o-C_α) is plotted against the difference in composition between precipitate and matrix (C_β-C_α) in a lever rule diagram, shown in Fig. 4. The slopes of the best-fit lines for all elemental compositions give the volume fraction of the precipitate phases in the two alloys: 17.6 ± 1.7% for B2 and 20.5 ± 1.6% for L2$_1$ in FBB8-2Ti and 22.1 ± 1.0% for L2$_1$ in FBB8-4Ti (the error is a standard deviation (σ) from the value in the fitted line). This lever rule diagram is an estimation assuming a single phase precipitate. In the mixture of B2 and L2$_1$ phases for FBB8-2Ti, the precipitate volume fraction is positioned between the two phases' volume fraction. In the lever rule diagram, Fig. 4, the points for Ti and Al deviate from the best-fit line. This represents the progression of Ti and Al separating into their eventual equilibrium concentrations in the B2 and L2$_1$ phases as the transition from the B2 to the L2$_1$ structure involves ordering of the Al and Ti atoms on the Al sub-lattice of the B2 structure. After homogenization at 1200 °C for 0.5 h, the precipitate has 36.8Ni-33.9Al-18.3Fe-9.75Ti-0.37Mo-0.65Cr (at.%) composition as measured by APT [35]. The initial Ti concentration of the precipitate, 9.75 at.%, in the homogenized sample is intermediate between the two compositions of the B2 and L2$_1$ phases, 6.76 and 13.13 at.%. The Al concentration also evolves from 33.9% in the homogenized structure to 37.5 and 32.2% in the B2 and L2$_1$ precipitates, respectively. It is also interesting that the volume fraction (V_f) increases as the phases present in the matrix evolve upon Ti addition from B2 alone (V_f = 13 ± 1% in Ti-free FBB8 [20]), to B2 + L2$_1$ (V_f = 19.6% in FBB8-2Ti), and to L2$_1$ alone (V_f = 22.1 ± 1.0% in FBB8-4Ti). This means that the precipitate volume fraction, which increases upon adding Ti to FBB8 by developing L2$_1$ phase in B2-structured precipitates (hierarchical structure), may also be a contributing factor to precipitate strengthening at high temperature (creep resistance) additionally to increasing the lattice parameter mismatches between the ferritic matrix and the ordered

Table 2
Composition (at. %) of FBB8–4Ti alloy (measured by direct-current plasma mass spectroscopy after casting) and of constitutive phases, matrix, B2 and L2$_1$ (after aging treatment at 700 °C for 100 h, as determined by atom probe tomography, all in at. %). Uncertainties are represented by the standard deviation (σ) from the counting statistics measurement series (at.%). Partitioning ratios and their errors (sum of relative errors of concentration) are also given.

| Phase	Fe	Ni	Al	Ti	Mo	Cr	Zr
Nominal composition	63.11	9.41	10.93	4.22	1.86	10.32	0.15
Matrix (bcc)	75.56 ± 0.30	2.03 ± 0.09	6.83 ± 0.17	0.36 ± 0.04	2.09 ± 0.09	13.08 ± 0.21	0.02 ± 0.01
Precipitates (L2$_1$)	19.25 ± 0.27	33.51 ± 0.31	27.48 ± 0.28	18.21 ± 0.26	0.88 ± 0.06	0.58 ± 0.05	0.05 ± 0.02
Partitioning ratio (L2$_1$/bcc)	0.2 ± 0.01	16.0 ± 1.53	4.0 ± 0.11	50.1 ± 5.25	0.4 ± 0.03	0.1 ± 0.01	3.3 ± 0.9
Sub-precipitates	76.15 ± 0.75	2.84 ± 0.27	7.02 ± 0.44	0.37 ± 0.10	2.0 ± 0.2	11.6 ± 0.5	0.02 ± 0.01
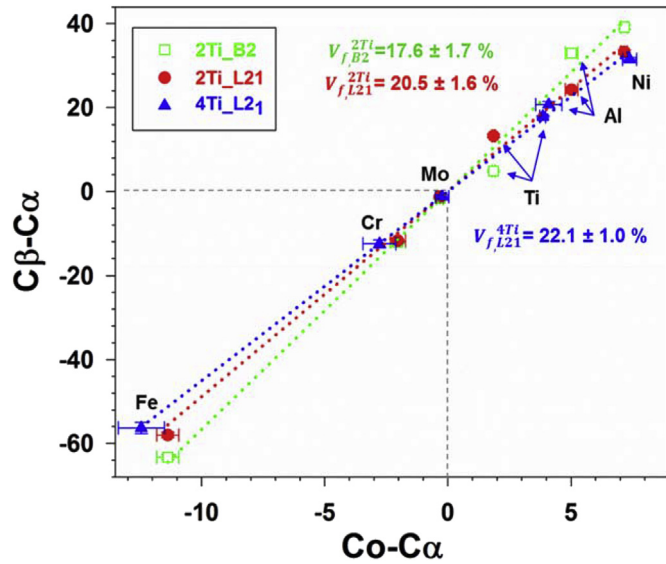
Fig. 4. Lever rule diagram to determine precipitate volume fraction (V_f) using APT concentration measurements. For each element, the difference between the overall alloy concentration (C_o) and the matrix concentration (C_α) is plotted vs. the difference in compositions between precipitate (C_β) and matrix (C_α). From this lever rule diagram, the volume fraction of B2 phase $\left(V_{f,2Ti}^{B2}\right)$ is found as 17.6 ± 1.7% and that of L2$_1$ phase $\left(V_{f,2Ti}^{L21}\right)$ as 20.5 ± 1.6% for FBB8-2Ti. The volume fraction of the L2$_1$ phase in the FBB8-4Ti $\left(V_{f,4Ti}^{L21}\right)$ is ~22.1 ± 1.0%. The errors are standard deviations (σ) from the value of the fitted line.

precipitates. As measured in creep experiments [15], FBB8-2Ti with the B2/L2$_1$ hierarchical precipitate structure displays very much higher creep resistance than Ti-free FBB8 with single phase B2 precipitates (creep threshold stress is tripled from 60 to 179 MPa). In FBB8-4Ti with near fully L2$_1$ precipitates and has highest volume fraction ($V_f = 22.1 \pm 1.0\%$), however, the creep threshold stress is somewhat reduced, 170 MPa, by the presence of a misfit dislocation network at the matrix-precipitate interface, indicating a semi-coherent interface between precipitates and the bcc-Fe matrix.

4.2. Thermodynamic evaluation for hierarchical sub-precipitate formation in precipitate

The heretical structure B2/L2$_1$ phase in the precipitates can be discussed from the pseudo-binary phase-diagram between (Ni,Fe) Al and (Ni,Fe)Ti [18,47], as shown in Fig. 5. It should be noted that the composition of matrix of FBB8-2Ti after homogenization at 1200 °C for 0.5 h is 77.2Fe-1.34Ni-6.3Al-0.33Ti-2.26Mo-12.5Cr at.% [35]. This is nearly identical to its matrix composition after aging at 700 °C for 100 h, Table 1. This means that the evolution of the volume fraction and composition of the precipitates occurs very locally, with little compositional changes in the matrix. For phase separations in precipitates, the TEM-APT correlative method [48–51] can clarify both the structure and composition of precipitate. Even though, such correlative experiments were not carried out here, phase separation between B2 and L2$_1$ phases within precipitates in the FBB8-2Ti sample is quite convincingly explained by Ti partitioning and ordering which is clearly seen in SADP and DF images in our TEM analysis, Fig. 1.

In the pseudo-binary phase-diagram between (Ni,Fe)Al and (Ni,Fe)Ti, Fig. 5, miscibility gaps exist on both the B2-NiAl and the B2-NiTi sides of the diagram and the two resulting B2-L2$_1$ two-phase regions are widening with decreasing temperature. The dotted lines represents the critical temperature (T_c), for a given
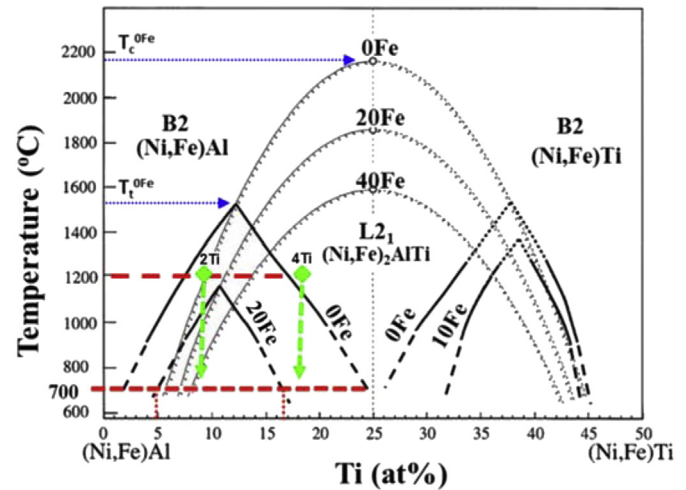
Fig. 5. Phase equilibria between the B2 and L2$_1$ phases in the (Ni,Fe)Al-(Ni,Fe)$_2$AlTi-(Ni,Fe)Ti pseudo-binary system with various Fe concentrations, reproduced from Ref. [18]. The phase separation inside precipitate is indicated by the miscibility gab between B2-L2$_1$ phases. The red dot line indicates an iso-temperature line at 700 °C and green diamond symbols indicate a positions of Ti concentration after homogenization at 1200 °C [35]. (For interpretation of the references to colour in this figure legend, the reader is referred to the web version of this article.)

composition, at which the ordering reaction from B2 to L2$_1$ phase takes place. In this system, the transition is achieved by ordering of the Al and Ti atoms on the Al sub-lattice of the B2 structure. The tri-critical temperature (T_t) point in the Ni-Al-Ti system corresponds to the B2-NiAl and L2$_1$-Ni$_2$AlTi reaction at the intersection of the miscibility gap and the continuous ordering line. The T_c and T_t for 0 at.% Fe for the B2-NiAl and L2$_1$-Ni$_2$AlTi reactions are marked as T_c^{0Fe} and T_t^{0Fe} in Fig. 5 and they decrease when adding Fe. During cooling from the 1200 °C homogenization temperature of the FBB8+2 and 4Ti steels, the Ti concentration within the precipitates determines which majority phase is created in the precipitates. If the initial concentration of Ti is higher than the T_t concentration, it forms a L2$_1$ structure; otherwise, a B2 structure first forms, and then evolves into a hierarchical B2/L2$_1$ microstructure. However, Fe additions to the alloy change the phase equilibrium and miscibility-gap between the B2-NiAl and L2$_1$-Ni$_2$AlTi phases. With increasing Fe concentration, as shown in the phase diagram of Fig. 5, the stability region of the L2$_1$ phase shrinks as do the B2-L2$_1$ two-phase regions on both the Al- and Ti-rich sides of the diagram. It is indicated by the decrease of both maxima given by T_c and T_t (marked on Fig. 5 for 0% Fe). For 20 at% Fe, the B2-L2$_1$ two-phase regions disappear at homogenization temperature of 1200 °C, i.e. the T_t temperature sinks below 1200 °C. At the aging temperature of 700 °C, the volume fraction and Ti concentration of B2 and L2$_1$ phases are delineated by the dotted red line in Fig. 5. The equilibrium concentrations of Ti in the phase diagram are ~6% in the B2 phase and ~17% in L2$_1$ phase at the aging temperature of 700 °C with 20 at.% Fe, as shown with vertical lines in Fig. 5. These equilibrium Ti concentrations are in general agreement with the APT values measured for the precipitates of FBB8-2Ti (see Table 1): 6.7 and 13 at.% in the B2 and L2$_1$ (sub-)precipitates, respectively. The discrepancy may be due to the presence of other alloying elements in the precipitates (i.e., Zr, Mo and Cr) and the possibility that equilibrium has not yet been fully reached.

The Ti concentration in the L2$_1$ precipitates of FBB8-4Ti is 18.2 at.% and falls in the L2$_1$-stabilized region in the pseudo-binary (Ni,Fe)Al−(Ni,Fe)$_2$AlTi phase-diagram from the homogenization temperature of 1200 °C. Thus, L2$_1$ precipitates are fully formed after homogenization and the phase separation during aging of FBB8-4Ti

is different from that of FBB8-2Ti as Fe-Cr-rich, bcc sub-precipitates, with composition nearly identical to that of the matrix, form within the L2$_1$ precipitates. This may be due to (i) Ti concentration is in the L2$_1$ stabilized region in the Ni-Al-Ti ternary diagram, (ii) Fe concentration being higher (19.3 at.%) in the L2$_1$ precipitates of the FBB8-4Ti than in those of FBB8-2Ti (17.4 at.%.). As shown above in the APT experiments, the Fe concentration increases along with Ti concentration in the L2$_1$ structure; the Fe decreases the stability of both the L2$_1$ and B2 structures, as possibly do other bcc partitioning alloying elements such as Cr and Mo. Thus, it appears that the bcc-structure is more stable than the B2 structure when forming within the L2$_1$ precipitates for FBB8-4Ti, resulting in the observed different hierarchical microstructure for the precipitates than in FBB8-2Ti. The excess of Fe, Cr and Mo in L2$_1$ out-diffuses to bcc matrix or forms a bcc phase inside L2$_1$ phase precipitate.

4.3. Kinetic path of hierarchical microstructure

In this section, we discuss the nucleation and growth of hierarchical precipitate in the FBB8-Ti ferritic alloy. In the as-homogenized alloy at 1200 °C, the microstructure is that of a typical precipitation-strengthened ferritic alloy [20,52,53], where single phase B2 or L2$_1$ precipitates are coherently or semi-coherently embedded in the bcc-Fe matrix. The presence of Al in the matrix, 6.5 at.% in 2Ti and 6.8 at.% in 4Ti-FBB8 alloy, stabilizes the bcc-phase, and the initial microstructure of precipitates and bcc-Fe matrix is created during cooling from the liquid phase [17,54]. This also occurs in very fast cooling experiments from the solidus, via the melt-spinning method, where B2 or L2$_1$ precipitates are obtained in the Fe bcc-matrix [13,55], implying that the B2 or L2$_1$ phases are already stable from the liquidus line [56,57]. When the Ti concentration is < 15 at.% Ti in the Ni-Al-Ti phase diagram, Fig. 5, rapid solidification from the liquid shows that the B2 phase is more stable than the L2$_1$ phase and that the L2$_1$ phase is nucleated from the B2 phase.

In early-stage aging at 700 °C, the B2-phase precipitate of FBB8-2Ti contains supersaturated Ti, and the L2$_1$-Ni$_2$TiAl phase is nucleated by Ti ordering and replacing half of the Al atoms in the B2 lattice. The nucleation of L2$_1$/B2 hierarchical structure in the precipitates occurs by wetting or heterogeneous nucleation on B2 anti-phase domain boundaries (APBs) because the high APB energy of the B2 structure, 0.5 J/m^2 [58], can reduce the energy barrier between B2 and L2$_1$ phases for nucleation [13,56]. Furthermore, a decrease in interface energies between B2 and L2$_1$ for temperatures above 350 °C plays a role in the development of hierarchical microstructures within the precipitates, which varies from 50 mJ/m^2 at 0 K to 11 mJ/m^2 at 973 K, as determined from canonical Monte-Carlo simulations [13]. By reducing the interface energy between the B2 and L2$_1$ phases, the nucleation and growth of sub-precipitates in the main precipitates can be promoted. The coarsening of sub-precipitate is not well represented in this single aging time study [13,35]. The hierarchical structure is, however, already well developed in a sample aged at 700 °C for 100 h and the compositions are similar to B2 and L2$_1$-alloys in the Ni-Al-Ti phase diagram [18]. The precipitation of L2$_1$-Ni$_2$AlTi in B2-NiAl requires not only segregation of Ti to localized regions of high concentration but also arrangement of Ti on specific lattice sites. The nucleation at APB and further development of L2$_1$ phase in the B2 phase are consistent with the homogenous nucleation growth, which is also supported by canonical Monte-Carlo simulations [13]. The bcc sub-precipitate in L2$_1$ precipitate is similar to the formation of L2$_1$ sub-precipitates in the B2 phase [55]. The L2$_1$ precipitates in the FBB8-4Ti alloy are fully formed after homogenization, and the bcc/L2$_1$ phase separation takes place within the L2$_1$ precipitates during aging at 700 °C. As shown above in the APT experiments, Fe, Cr and

Mo supersaturated in the L2$_1$ phase out-diffuse to the bcc matrix or forms a bcc phase within the L2$_1$ precipitates.

5. Conclusions

The ferritic steel FBB8 (Fe−10.0Cr−9.9-10.5Ni−5.4-5.8Al−3.1-3.5Mo−0.18-0.31Zr−0-0.005B, wt.%) shows, after aging at 700 °C, single-phase B2 precipitates. The precipitates, upon addition of 2 and 4 wt% of Ti, remain B2 or become L2$_1$, respectively, but both display sub-precipitates. These hierarchical precipitates are studied here, utilizing transmission electron microscopy (TEM) and atom probe tomography (APT), leading to the following conclusions:

- Dark-field (DF) TEM images reveal, in both FBB8-2Ti and -4Ti, the hierarchical microstructure of the precipitate. FBB8-2Ti exhibits cuboidal (50−100 nm in size), coherent B2 precipitates, with an interfacial alignment towards a cube-on-cube orientation, containing L2$_1$-Ni$_2$TiAl sub-precipitates. By contrast, FBB8-4Ti shows L2$_1$-ordered precipitates (200−500 nm in size) containing plate-like sub-precipitate. Thus, these relatively small Ti additions to FBB8 have a strong effect on the microstructure of the precipitates.
- 3D APT analysis of FBB8-2Ti further clarifies the B2/L2$_1$ hierarchical microstructure of the precipitates. Fe, Cr and Mo are strongly partitioned to the matrix phase, whereas Ni, Al, Ti and Zr are mainly concentrated into the B2 and L2$_1$ (sub)-precipitates. Between the B2 and L2$_1$ precipitates, Ti, Fe, Mo, Cr and Zr are enriched in the L2$_1$ sub-precipitates (and consequently Ni and Al are depleted). Fe is also preferentially partitioned into the L2$_1$ phase rather than the B2 phase and the sum of the Ni and Fe concentrations is nearly 50 at.% in both B2 and L2$_1$ structure. This may reflect that Fe, occupying the Ni sub-lattice in the L2$_1$-Ni$_2$TiAl structure, has higher affinity for Ti than for Al.
- 3D APT analysis of FBB8-4Ti shows L2$_1$ precipitate containing sub-precipitates whose composition is nearly identical to that of the bcc matrix of the steel. These Fe- and Cr-rich sub-precipitates within the L2$_1$ precipitates are thus likely disordered (with the same bcc structure as the matrix), unlike the ordered sub-precipitates in FBB8-2Ti. As they grow during aging, these matrix-like sub-precipitates may be able to split the L2$_1$ precipitates, effectively decreasing their size, which may prevent the loss of mechanical strength associated with long-term coarsening in alloys with single-phase precipitates.
- The volume fraction of precipitates is estimated by the lever rule using the measured compositions in the APT experiment. When ignoring the secondary precipitates and assuming that the alloying elements evenly partition to every precipitate, the volume fraction of the B2 precipitates in FBB8-2Ti is 17.6 ± 1.7%, and that of the L2$_1$ precipitates is 20.5 ± 1.6%. The volume fraction of L2$_1$ precipitates in FBB8-4Ti is ~22.1 ± 1.0%. The deviation of Ti and Al concentration from the best fit lines in the lever rule diagram, Fig. 4, represents the progression of Ti and Al partitioning into the equilibrium concentration between B2 and L2$_1$ phases.
- The hierarchical structure of the B2−L2$_1$ and L2$_1$-bcc precipitates is discussed in the light of Ti ordering and phase separation using a published pseudo-binary phase-diagram between (Ni,Fe)Al and (Ni,Fe)Ti, Fig. 5. The volume fraction and Ti concentration of B2 and L2$_1$ phases in FBB8-2Ti is determined by the iso-temperature intersection of the miscibility gap at 700 °C from this diagram, and the predicted Ti concentration of both phases is in reasonable agreement with APT measurements. In FBB8-4Ti, the appearance of Fe-Cr rich bcc sub-precipitates may be due to the high Fe concentration in the

L2$_1$ main precipitates, which can decrease the stability of both L2$_1$ and B2 phases.

Acknowledgements

Appendix A. Supplementary data

Supplementary data related to this article can be found at https://doi.org/10.1016/j.actamat.2017.11.013.

References

[1] H. Bhadeshia, Design of ferritic creep-resistant steels, Isij Int. 41 (2001) 626−640.

[2] F. Masuyama, History of power plants and progress in heat resistant steels, Isij Int. 41 (2001) 612−625.

[3] R.L. Klueh, Elevated temperature ferritic and martensitic steels and their application to future nuclear reactors, Int. Mater Rev. 50 (2005) 287−310.

[4] B. Weiss, R. Stickler, Phase instabilities during high-temperature exposure of 316 austenitic stainless-steel, Metall. Trans. 3 (1972) 851−866.

[5] M. Taneike, F. Abe, K. Sawada, Creep-strengthening of steel at high temperatures using nano-sized carbonitride dispersions, Nature 424 (2003) 294−296.

[6] H. Leitner, M. Schober, R. Schnitzer, Splitting phenomenon in the precipitation evolution in an Fe-Ni-Al-Ti-Cr stainless steel, Acta Mater. 58 (2010) 1261−1269.

[7] O. Prat, J. Garcia, D. Rojas, C. Carrasco, G. Inden, Investigations on the growth kinetics of Laves phase precipitates in 12% Cr creep-resistant steels: Experimental and DICTRA calculations, Acta Mater. 58 (2010) 6142−6153.

[8] P.R. Strutt, R.S. Polvani, B.H. Kear, Dynamic strain aging in creep of beta-NiAl, Scr. Metall. 7 (1973) 949−954.

[9] S.M. Zhu, S.C. Tjong, J.K.L. Lai, Creep behavior of a beta' (NiAl) precipitation strengthened ferritic Fe-Cr-Ni-Al alloy, Acta Mater. 46 (1998) 2969−2976.

[10] C. Stallybrass, G. Sauthoff, Ferritic Fe-Al-Ni-Cr alloys with coherent precipitates for high-temperature applications, Mat. Sci. Eng. a-Struct 387 (2004) 985−990.

[11] Z.K. Teng, F. Zhang, M.K. Miller, C.T. Liu, S. Huang, Y.T. Chou, R.H. Tien, Y.A. Chang, P.K. Liaw, New NiAl-strengthened ferritic steels with balanced creep resistance and ductility designed by coupling thermodynamic calculations with focused experiments, Intermetallics 29 (2012) 110−115.

[12] J. Jung, G. Ghosh, G.B. Olson, A comparative study of precipitation behavior of Heusler phase (Ni2TiAl) from B2-TiNi in Ni-Ti-Al and Ni-Ti-Al-X (X = Hf, Pd, Pt, Zr) alloys, Acta Mater. 51 (2003) 6341−6357.

[13] C.H. Liebscher, V.R. Radmilovic, U. Dahmen, N.Q. Vo, D.C. Dunand, M. Asta, G. Ghosh, A hierarchical microstructure due to chemical ordering in the bcc lattice: early stages of formation in a ferritic Fe-Al-Cr-Ni-Ti alloy, Acta Mater. 92 (2015) 220−232.

[14] G. Song, Z. Sun, L. Li, X. Xu, M. Rawlings, C.H. Liebscher, B. Clausen, J. Poplawsky, D.N. Leonard, S. Huang, Z. Teng, C.T. Liu, M.D. Asta, Y. Gao, D.C. Dunand, G. Ghosh, M. Chen, M.E. Fine, P.K. Liaw, Ferritic alloys with extreme creep resistance via coherent hierarchical precipitates, Sci. Rep-Uk 5 (2015).

[15] M.J.S. Rawlings, C.H. Liebscher, M. Asta, D.C. Dunand, Effect of titanium additions upon microstructure and properties of precipitation-strengthened Fe-Ni-Al-Cr ferritic alloys, Acta Mater. 128 (2017) 103−112.

[16] A.J. Bradley, Microscopical studies on the iron nickel aluminium system 2. The breakdown of the body-centred cubic lattice, J. Iron Steel I 168 (1951) 233−244.

[17] S.M. Hao, T. Takayama, K. Ishida, T. Nishizawa, Miscibility gap in Fe-Ni-Al and Fe-Ni-Al-Co systems, Metall. Trans. A 15 (1984) 1819−1828.

[18] R. Kainuma, K. Urushiyama, K. Ishikawa, C.C. Jia, I. Ohnuma, K. Ishida, Ordering and phase separation in bcc aluminides of the Ni-Fe-Al-Ti system, Mat. Sci. Eng. a-Struct 240 (1997) 235−244.

[19] S.H. Jiang, H. Wang, Y. Wu, X.J. Liu, H.H. Chen, M.J. Yao, B. Gault, D. Ponge, D. Raabe, A. Hirata, M.W. Chen, Y.D. Wang, Z.P. Lu, Ultrastrong steel via minimal lattice misfit and high-density nanoprecipitation, Nature 544 (2017) 460−464.

[20] N.Q. Vo, C.H. Liebscher, M.J.S. Rawlings, M. Asta, D.C. Dunand, Creep properties and microstructure of a precipitation-strengthened ferritic Fe-Al-Ni-Cr alloy, Acta Mater. 71 (2014) 89−99.

[21] Y.X. Zhao, Q.H. Fang, Y.W. Liu, P.H. Wen, Y. Liu, Creep behavior as dislocation climb over NiAl nanoprecipitates in ferritic alloy: the effects of interface stresses and temperature, Int. J. Plast. 69 (2015) 89−101.

[22] P.R. Strutt, R.S. Polvani, J.C. Ingram, Creep-behavior of heusler type structure alloy Ni2AlTi, Metall. Trans. A 7 (1976) 23−31.

[23] D.A. Grose, G.S. Ansell, The influence of coherency strain on the elevated-temperature tensile behavior of Ni-15cr-Al-Ti-Mo alloys, Metall. Trans. A 12 (1981) 1631−1645.

[24] G. Song, Z.Q. Sun, B. Clausen, P.K. Liaw, Microstructural characteristics of a Ni2TiAl-precipitate-strengthened ferritic alloy, J. Alloy Compd. 693 (2017) 921−928.

[25] R.X. Hu, H.N. Su, P. Nash, Enthalpies of formation and lattice parameters of B2 phases in Al-Ni-X systems, Pure Appl. Chem. 79 (2007) 1653−1673.

[26] X.L. Yan, A. Grytsiv, P. Rogl, V. Pomjakushin, M. Palm, The heusler phase Ti-25(Fe50-xNix)Al-25 (0 <= x <= 50); structure and constitution, J. Phase Equilib. Diff 29 (2008) 500−508.

[27] I. Ohnuma, C.G. Schon, R. Kainuma, G. Inden, K. Ishida, Ordering and phase separation in the b.c.c. phase of the Fe-Al-Ti system, Acta Mater. 46 (1998) 2083−2094.

[28] Z.Q. Sun, G. Song, J. Ilavsky, G. Ghosh, P.K. Liaw, Nano-sized precipitate stability and its controlling factors in a NiAl-strengthened ferritic alloy, Sci. Rep-Uk 5 (2015).

[29] Z.K. Teng, C.T. Liu, G. Ghosh, P.K. Liaw, M.E. Fine, Effects of Al on the microstructure and ductility of NiAl-strengthened ferritic steels at room temperature, Intermetallics 18 (2010) 1437−1443.

[30] G. Marcon, R. Peffen, H. Lemaire, Fe-Ni-Al phase-diagram in AlNi type permanent-magnets related area, IEEE Trans. Magn. 14 (1987) 685−687.

[31] P. Nash, W.W. Liang, Phase-equilibria in the Ni-Al-Ti system at 1173 K, Metall. Trans. A 16 (1985) 319−322.

[32] F. Vogel, N. Wanderka, S. Matsumura, J. Banhart, Early stages of decomposition within the gamma ' phase of a Ni-Al-Ti model alloy, Intermetallics 22 (2012) 226−230.

[33] J.S. Van Sluytman, T.M. Pollock, Optimal precipitate shapes in nickel-base gamma-gamma ' alloys, Acta Mater. 60 (2012) 1771−1783.

[34] F. Vogel, N. Wanderka, Z. Balogh, M. Ibrahim, P. Stender, G. Schmitz, J. Banhart, Mapping the evolution of hierarchical microstructures in a Ni-based superalloy, Nat. Commun. 4 (2013).

[35] G.A. Song, Z.Q. Sun, J.D. Poplawsky, Y.F. Gao, P.K. Liaw, Microstructural evolution of single Ni2TiAl or hierarchical NiAl/Ni2TiAl precipitates in Fe-Ni-Al-Cr-Ti ferritic alloys during thermal treatment for elevated-temperature applications, Acta Mater. 127 (2017) 1−16.

[36] D.N. Seidman, Three-dimensional atom-probe tomography: advances and applications, Annu. Rev. Mater Res. 37 (2007) 127−158.

[37] T.F. Kelly, M.K. Miller, Atom probe tomography, Rev. Sci. Instrum. 78 (2007) 1−20.

[38] B. Gault, M.P. Moody, Julie M. Cairney, S.P. Ringer, Atom Probe Microscopy, Springer Series in Materials Science, 2012.

[39] M.K. Miller, R.G. Forbes, Atom Probe Tomography: the Local Electrode Atom Probe, Springer, 2014.

[40] O.C. Hellman, J.A. Vandenbroucke, J. Rusing, D. Isheim, D.N. Seidman, Analysis of three-dimensional atom-probe data by the proximity histogram, Microsc. Microanal. 6 (2000) 437−444.

[41] G. Song, Z.Q. Sun, L. Li, B. Clausen, S.Y. Zhang, Y.F. Gao, P.K. Liaw, High temperature deformation mechanism in hierarchical and single precipitate strengthened ferritic alloys by in situ neutron diffraction studies, Sci. Rep-Uk 7 (2017).

[42] K.E. Yoon, R.D. Noebe, O.C. Hellman, D.N. Seidman, Dependence of interfacial excess on the threshold value of the isoconcentration surface, Surf. Interface Anal. 36 (2004) 594−597.

[43] P.W. Voorhees, G.B. McFadden, W.C. Johnson, On the morphological development of 2nd-phase particles in elastically-stressed solids, Acta Metall. Mater 40 (1992) 2979−2992.

[44] L.G. Parratt, Probability and Experimental Errors in Science, John Wiley & Sons, 1961. An Elementary Survey.

[45] A. Leo, C. Hansch, D. Elkins, Partition coefficients and their uses, Chem. Rev. 71 (1971) 525−616.

[46] O.C. Hellman, J.A. Vandenbroucke, J. Rusing, D. Isheim, D.N. Seidman, Identification of 2D boundaries from 3D atom probe data, and spatial correlation of atomic distributions with interfaces, Multiscale Phenom. Materials-Experiments Model. 578 (2000) 395−400, 491.

[47] K. Ishikawa, R. Kainuma, I. Ohnuma, K. Aoki, K. Ishida, Phase stability of the X2AlTi (X : Fe, Co, Ni and Cu) Heusler and B2-type intermetallic compounds, Acta Mater. 50 (2002) 2233—2243.

[48] I. Arslan, E.A. Marquis, M. Homer, M.A. Hekmaty, N.C. Bartelt, Towards better 3-D reconstructions by combining electron tomography and atom-probe to-mography, Ultramicroscopy 108 (2008) 1579—1585.

[49] B.P. Gorman, D. Diercks, N. Salmon, E. Stach, G. Amador, C. Hartfield, Hardware and techniques for cross-correlative TEM and atom probe analysis, Microsc. Today (2008) 42—47.

[50] S.I. Baik, X. Yin, D.N. Seidman, Correlative atom-probe tomography and transmission electron microscope study of a chemical transition in a spinel on an oxidized nickel-based superalloy, Scr. Mater 68 (2013) 909—912.

[51] F. Vurpillot, W. Lefebvre, J.M. Cairney, C. Oberdorfer, B.P. Geiser, K. Rajan, Advanced volume reconstruction and data mining methods in atom probe tomography, Mrs Bull. 41 (2016) 46—51.

[52] H.A. Calderon, M.E. Fine, J.R. Weertman, Coarsening and morphology of β'-particles in Fe-Ni-Al-Mo ferritic alloys, Metall. Trans. A 19 (1988) 1135—1146.

[53] Z.K. Teng, M.K. Miller, G. Ghosh, C.T. Liu, S. Huang, K.F. Russell, M.E. Fine, P.K. Liaw, Characterization of nanoscale NiAl-type precipitates in a ferritic steel by electron microscopy and atom probe tomography, Scr. Mater 63 (2010) 61—64.

[54] S.M. Hao, K. Ishida, T. Nishizawa, Role of alloying elements in phase-decomposition in AlNico magnet alloys, Metall. Trans. A 16 (1985) 179—185.

[55] C.H. Liebscher, V. Radmilovic, U. Dahmen, M. Asta, G. Ghosh, On the formation of hierarchically structured L2$_1$-Ni$_2$TiAl type precipitates in a ferritic alloy, J. Mater Sci. 48 (2013) 2067—2075.

[56] W.J. Boettinger, L.A. Bendersky, F.S. Biancaniello, J.W. Cahn, Rapid solidifica-tion and ordering of B2 and L2$_1$ phases in the NiAl-NiTi ystem, Mater Sci. Eng. 98 (1988) 273—276.

[57] A.W. Wilson, J.M. Howe, A. Garg, R.D. Noebe, TEM study of beta' precipitation in Ni-Al-Ti alloys, Mat. Sci. Eng. a-Struct 289 (2000) 162—171.

[58] R.D. Noebe, R.R. Bowman, M.V. Nathal, Physical and mechanical-properties of the B2 compound NiAl, Int. Mater Rev. 38 (1993) 193—232.